

Data-Augmented Few-Shot Neural Stencil Emulation for System Identification of Computer Models

Sanket Jantre¹ Deepak Akhare² Xiaoning Qian^{1,3} Nathan M. Urban¹

¹Brookhaven National Laboratory ²University of Notre Dame ³Texas A&M University
 {sjantre, xqian1, nurban}@bnl.gov {dakhare}@nd.edu {xqian}@tamu.edu

Abstract

Partial differential equations (PDEs) underpin the modeling of many natural and engineered systems. It can be convenient to express such models as neural PDEs rather than using traditional numerical PDE solvers by replacing part or all of the PDE’s governing equations with a neural network representation. Neural PDEs are often easier to differentiate, linearize, reduce, or use for uncertainty quantification than the original numerical solver. They are usually trained on solution trajectories obtained by long time integration of the PDE solver. Here we propose a more sample-efficient data-augmentation strategy for generating neural PDE training data from a computer model by space-filling sampling of local “stencil” states. This approach removes a large degree of spatiotemporal redundancy present in trajectory data and oversamples states that may be rarely visited but help the neural PDE generalize across the state space. We demonstrate that accurate neural PDE stencil operators can be learned from synthetic training data generated by the computational equivalent of 10 timesteps’ worth of numerical simulation. Accuracy is further improved if we assume access to a single full-trajectory simulation from the computer model, which is typically available in practice. Across several PDE systems, we show that our data-augmented synthetic stencil data yield better trained neural stencil operators, with clear performance gains compared with naïvely sampled stencil data from simulation trajectories.

1 Introduction

Mechanistic computer models, often formulated as partial differential equations (PDEs), are pivotal for simulating complex physical systems across fluid dynamics [1, 2], climate modeling [3, 4], biology [5], and chemistry [6]. These PDE-based models simulate underlying governing processes to predict complex dynamics, informing decision-making, system design, and intervention strategies. In practice, PDEs often lack analytical solutions and rely on classical numerical methods such as finite difference methods (FDM) [7, 8], finite volume methods (FVM) [9, 10], and finite element methods (FEM) [11, 12]. These discretization approaches approximate differential operators via handcrafted stencils, balancing simplicity (FDM), local conservation (FVM), and geometric flexibility (FEM). For applications requiring increased accuracy, high-order schemes like discontinuous Galerkin and spectral methods have emerged [13, 14], at higher computational cost and complexity. All of these approaches rely on correctly specifying the governing equations, a requirement that breaks down when the underlying physics are only partially known or prohibitively complex [15].

Emerging machine learning (ML) approaches seek to learn solution operators or surrogate models directly from data while retaining physical fidelity and improving flexibility and scalability [16–18]. Physics-informed neural networks (PINNs) [16, 19–21] embed PDE residuals into the loss, enabling mesh-free, often unsupervised training. Neural operators—e.g. DeepONets [22], Fourier Neural Operators (FNOs) [23]—learn mappings between infinite-dimensional function spaces, generalizing

across inputs without discretization. Despite strong promise, both approaches often endure slow or unstable convergence, spectral bias, and sensitivity to loss-weight choices [24]. Heuristics such as adaptive sampling [25, 26] and weight-update rules [27–29] mitigate specific failure modes, but broader challenges—especially efficient, few-shot learning of surrogates for forecasting—remain open.

An alternative to regression-style ML surrogates is neural differential equations (NDEs), which learn the governing equations or “right-hand-side” (RHS) of an ordinary (ODE) or partial differential equation with a neural network and make predictions by timestepping the learned equations using a numerical solver [30, 31]. When only part of the RHS is learned, the models are termed universal differential equations (UDEs) [32] or hybrid models [33–35]. NDEs—including neural ODEs (NODEs) and neural PDEs (NPDEs)—inherit the computational cost of simulation models because they are themselves ODE or PDE solvers, yet they offer advantages over (possibly physics-constrained) regression-type surrogates. Even when governing equations are known, recasting a large, complex simulation as an NPDE can simplify equation-level manipulation—for example, linearizing NPDE for stability analysis [36] or obtaining gradients via adjoint or automatic differentiation—relative to linearizing or differentiating the original codebase. When the true governing equations are not known but are imperfectly approximated by a simulator, an NDE emulator of that simulator can serve as a “prior” over unknown system dynamics that can be updated with measurements [37]. Moreover, intrusive model-reduction techniques can be applied directly to the NPDE to accelerate simulation while avoiding the software complexity of modifying a mature codebase [37–39]. Some approaches learn resolution-specific local discretizations for stable long-horizon rollouts on coarse grids [40], whereas autoregressive next-step predictors [17, 41] iteratively apply a neural network to advance the state—an approach akin to discrete flow-map learning under partial observation [42].

Learning the governing equations of PDE systems in neural representations can be viewed as a special form of system identification, and NPDEs/UDEs are commonly trained on long solution trajectories. When data are generated from a simulation code rather than experiments, we can greatly control the training data. Specifically, in a simulation, we can precisely control the initial and boundary conditions, domain size, grid resolution, timestep, and other numerics, enabling *designing* more sample-efficient training sets for system identification and neural PDE training. Yet PDE solutions exhibit strong spatiotemporal redundancy—neighboring cells and successive timesteps often contain very similar states—so long integrations expend compute on simulating states that provide little independent information about the system’s governing dynamics. We instead sample from a space-filling design of local stencil states, emphasizing statistically independent configurations and underrepresented regions of state space.

To achieve this, we observe that numerical PDE solvers are often implemented in terms of a *stencil operator*: a spatially discretized RHS of the PDE determining the evolution of a grid cell’s state as a function of the state vector in a local “stencil” neighborhood of that cell [43]. Due to locality and homogeneity of the PDE’s governing equations, the same stencil operation is applied at every grid cell at every timestep. Rather than collecting an ensemble of costly, high-dimensional solution trajectories, we learn this stencil mapping from large numbers of computationally inexpensive *stencil* evaluations of the PDE. Conceptually, this corresponds to running the simulator over the neighborhood of a single grid cell for a single timestep across a statistically designed collection of local states.

At the core of our proposed approach lies a **neural stencil emulator (NSE)** that performs system identification in function space: it infers the model structure or functional form of the PDE RHS directly from grid-cell simulation data. NSE training leverages large amounts of grid-cell-level simulation data that are inexpensive to generate and often with no more than a single simulation. This non-intrusive scheme combines the scalability of data-driven models with the interpretability of mechanistic stencils, yielding an efficient, physics-aware surrogate for PDE evolution.

Our contributions are as follows:

- We introduce the *Neural Stencil Emulator (NSE)*, a non-intrusive, data-driven system-identification framework that learns the governing equations of computer models from inexpensive stencil evaluations, enabling stable forecasting;
- We develop several data-augmentation strategies, including a novel PCA-based scheme, that improves our emulator’s sample efficiency and few-shot generalization to unseen initial conditions using only a handful of full-order simulation snapshots;
- We demonstrate NSE’s effectiveness in learning PDE dynamics across multiple PDE systems, achieving low errors relative to full-order solutions.

2 Preliminaries

In this paper, vectors and matrices are denoted by bold lowercase and uppercase letters, respectively.

2.1 Dynamical Model

Continuous formulation. Let $u(\mathbf{x}, t)$ denote a spatio-temporal variable at spatial location $\mathbf{x} \in \Omega = [0, L]^d$ and time $t \in [0, T]$. The evolution of u is governed by the nonlinear partial differential equation capturing the system dynamics via a nonlinear operator \mathcal{F} that parameterizes the time derivative $\partial u / \partial t$ and the initial condition $u(\mathbf{x}, t_0)$. Formally, such a PDE can be expressed as:

$$\frac{\partial u(\mathbf{x}, t)}{\partial t} = \mathcal{F}(u(\mathbf{x}, t)) \quad (\mathbf{x}, t) \in \Omega \times [0, T], \quad (1a)$$

$$u(\mathbf{x}, t_0) = u_0(\mathbf{x}) \quad \mathbf{x} \in \Omega, \quad (1b)$$

$$\mathcal{BC}(u(\mathbf{x}, t)) = 0 \quad (\mathbf{x}, t) \in \partial\Omega \times [0, T], \quad (1c)$$

where \mathcal{F} encodes the system dynamics and $\mathcal{BC}(\cdot)$ enforces the boundary condition applied on $\partial\Omega = \bigcup_{k=1}^d \{\mathbf{x} \in \mathbb{R}^d \mid 0 \leq x_j \leq L \text{ for all } j \neq k, x_k \in \{0, L\}\}$. Lastly, the initial condition $u(\mathbf{x}, t_0)$ completes the PDE formulation, enabling the solution of $u(\mathbf{x}, t)$ over time.

Space-time discretization. To solve the aforementioned PDE numerically, we discretize the spatial domain Ω on n grid points $\{\mathbf{x}_i\}_{i=1}^n$ and partition the temporal domain into uniform steps of size Δt . Setting $t_k = t_0 + k\Delta t$, we approximate the continuous $u(\mathbf{x}, t)$ variable by discretizing the state at t_k by $\mathbf{u}^{(k)} = \{u(\mathbf{x}_i, t_k)\}_{i=1}^n$. Accordingly, a first-order explicit scheme yields

$$\mathbf{u}^{(k+1)} = \mathbf{u}^{(k)} + \Delta t \mathbf{F}(\mathbf{u}^{(k)}), \quad \mathbf{F} : \mathbb{R}^n \rightarrow \mathbb{R}^n, \quad (2)$$

where \mathbf{F} is the discrete counterpart of \mathcal{F} .

2.2 System Identification

In a numerical method, a mechanistic PDE solver advances a discretized PDE state by integrating it in time. For example, an explicit 2D finite-difference solver with an Euler timestepping is implemented via a localized *stencil* operator \mathbf{F} as in the following pseudo-code:

```

for each time  $t$  do
  for each grid cell  $(i, j)$  do
     $u_{i,j}^{t+1} = u_{i,j}^t + \mathbf{F}(\mathbf{S}(u_{i,j}^t))\Delta t$ 
  end for
end for

```

Here, $u_{i,j}^t$ denotes the state at grid cell (i, j) and time t . $\mathbf{S}(\cdot)$ is the localized *stencil* at $u_{i,j}^t$: a set containing $u_{i,j}^t$ and its neighboring grid cells within the fixed domain of dependence defining the stencil operator. For example, a 5-point stencil at $u_{i,j}^t$ is a set $\{u_{i,j}^t, u_{i-1,j}^t, u_{i+1,j}^t, u_{i,j-1}^t, u_{i,j+1}^t\}$. Such stencils are used to approximate spatial derivatives at each grid cell.

3 Neural Stencil Emulator

In Equation (1), we ideally wish to recover the continuum PDE's RHS $\mathcal{F}(\cdot)$; but in practice we learn the discretized operator \mathbf{F} and implement it within a numerical solver. While \mathbf{F} is known analytically for simple PDEs, complex simulation codes often contain conditional logic, empirical closures, and other intricate parameterizations that preclude a closed-form stencil operator. This lack of an analytical expression for \mathbf{F} has traditionally limited the application of intrusive reduced-order models (ROMs) that require direct access to the governing equations.

Instead, we propose to learn a statistical representation of \mathbf{F} from PDE solution data, rendering model order reduction non-intrusive. Our approach treats \mathbf{F} as a black-box mapping

$$\mathbf{S}(u_{i,j}^t) \mapsto u_{i,j}^{t+1}, \quad u_{i,j}^{t+1} = u_{i,j}^t + \mathbf{F}(\mathbf{S}(u_{i,j}^t)) \Delta t,$$

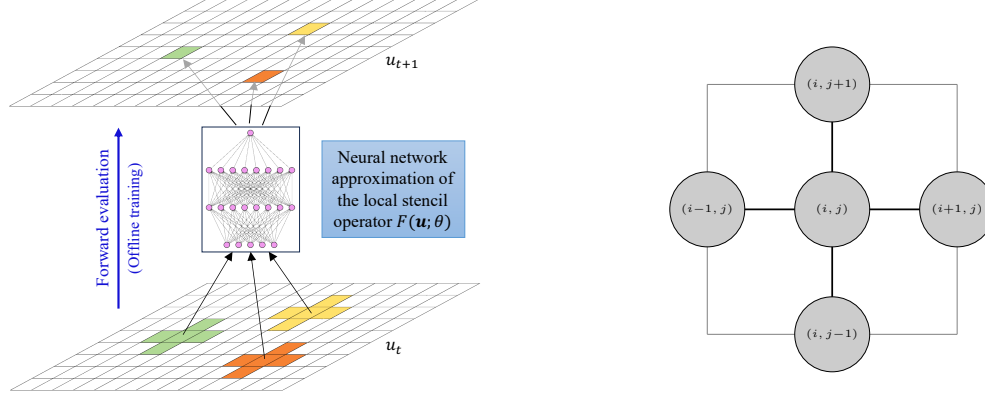


Figure 1: **Left.** A neural network learns the *stencil operator* \mathbf{F} : a mapping from a localized stencil of a state (\mathbf{S}) to its finite difference-based time derivative **Right.** A 5-point stencil schematic.

and trains a machine learning model $\hat{\mathbf{F}}_{\theta}$ with parameters θ to approximate it. We emphasize here that each stencil evaluation is low-dimensional (e.g. five or thirteen inputs plus one output), so a single high-fidelity simulation can produce a large number of training examples. For instance, a climate model with 10^6 grid cells over 10^6 timesteps yields $\sim 10^{12}$ stencil evaluations. Moreover, compared with existing state-of-the-art PDE surrogates based on PINN or neural operator learning that train on full spatial field instances, the stencil input is orders of magnitude lower dimensional, significantly reducing model size and training cost.

Various ML models can serve as $\hat{\mathbf{F}}_{\theta}(\cdot)$. One natural choice is Sparse Identification of Nonlinear Dynamics (SINDy) [44], which performs sparse regression on a set of nonlinear functions of state snapshots versus derivatives to identify the governing equations. While effective for “clean” PDE systems, SINDy’s basis may be too restrictive for the complex parameterizations in large-scale simulations. Here we instead use a neural-network-based stencil emulator, which is a more flexible and expressive functional approximator, for learning the RHS of high-dimensional PDEs (see Fig. 1), hence the name *neural stencil emulator* (NSE). We use a standard mean squared error loss over a dataset $\mathcal{D} = \{\mathbf{S}_z(u_z), \delta u_z\}_{z=1}^Z$, where $\delta u_z = (u_z^{t+1} - u_z^t)/\Delta t$ and z denotes spatial coordinate:

$$\mathcal{L}(\theta) = \frac{1}{Z} \sum_{z=1}^Z \|\hat{\mathbf{F}}_{\theta}(\mathbf{S}_z) - \delta u_z\|^2.$$

Optionally, physics-informed penalties (e.g. enforcing $\nabla \cdot \mathbf{u} = 0$) can be added.

Once trained, our NSE, $\hat{\mathbf{F}}_{\theta}$, replaces conventional timestepping, evolving the state while maintaining high accuracy relative to the original solver. By approximating \mathbf{F} directly—rather than the full state evolution—our surrogate remains non-intrusive and readily deployable alongside legacy solvers.

3.1 Adaptive Sampling Strategies

Stencil data from a single PDE trajectory are highly redundant: neighboring grid cells and successive timesteps are strongly correlated, so the *effective sample size* is far smaller than the total stencil evaluations obtained. To achieve desired sample efficiency training our NSE, we design space-filling and adaptive sampling strategies that (i) decorrelate stencil samples and (ii) increase coverage of rare but dynamically relevant states. By *synthetically* constructing localized stencil states and forcing the simulator to evaluate them, we avoid long integrations and enable few-shot learning. Hence, we use the forward model to obtain one-step labels $(\mathbf{S}, \delta \mathbf{u})$ for supervised learning of the stencil operator.

3.1.1 Pure strategies.

On-trajectory (“Short-Traj”) sampling. As a baseline, we use all available stencils from a given simulation trajectory when only short simulation is available. This *ergodic* sampler provides dynamically common states but yields strong space–time correlations and under-represents tail events.

Off-trajectory synthetic sampling. We introduce two synthetic stencil design and sampling schemes that expand coverage of rare (tail) states in NSE training data, particularly when only short simulation trajectories are available.

(i) **Random sampling.** Sample $\tilde{\mathbf{S}} \in [0, 1]^m$ via i.i.d. uniform draws or Sobol’ quasi-random sequences for space-filling coverage. Affinely rescale each state within a sampled stencil to the simulation data range. These i.i.d.-like inputs increase effective sample size and oversample corners of state space, promoting interpolation rather than extrapolation at training time for rare states.

(ii) **PCA-guided design.** Given a collection of actual on-trajectory stencils $\{\mathbf{S}_z\}$, we compute PCA using stencil mean $\boldsymbol{\mu}$, loading matrix $P \in \mathbb{R}^{m \times r}$, and PC scores $\mathbf{Z} = P^\top (\mathbf{S} - \boldsymbol{\mu})$. We use $r = m$ with $Z > m$ yielding full PCA. Next, we construct a hyper-rectangle in PC space using per-PC minima and maxima $[L_k, U_k]$ observed in \mathbf{Z} . Then perform the following steps:

1. Draw $\tilde{\mathbf{z}} \in [0, 1]^m$ via uniform or Sobol’ sampling and map to PC ranges: $\hat{\mathbf{z}}_k = L_k + \tilde{z}_k(U_k - L_k)$.
2. Back-project to the state space: $\hat{\mathbf{S}} = \boldsymbol{\mu} + P\hat{\mathbf{z}}$.
3. Filter out stencil samples outside simulation data range (applying physical constraints).
4. Repeat until the desired number of synthetic stencil states are collected.

This targets high-variance directions while retaining plausibility inherited from the empirical PCs.

3.1.2 Mixed strategies.

To balance frequent and rare regimes, we form a mixture sampler

$$q_\lambda = (1 - \lambda) p_{\text{ergodic}} + \lambda r_{\text{synthetic}},$$

where $r_{\text{synthetic}}$ is either Random or PCA-guided.

On-trajectory downsampling. A single long full-order simulation can produce millions of near-duplicate stencils. In our mixed strategies, we assume access to one such run and first downsample its stencil states (uniformly in space–time) to reduce correlation (Fig. 2). Next, we assume that we have a small additional compute budget to further augment the downsampled set by evaluating an equal-sized batch obtained via one of four options: (a) a short burst from a new initialization, (b) a short extension from the run’s terminal state, (c) one-step evaluations of synthetically designed random stencils, or (d) one-step evaluations of PCA-guided synthetic stencils.

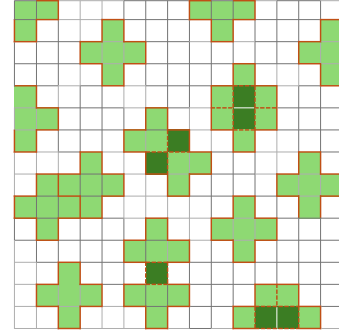


Figure 2: **On-trajectory downsampling.** We downsample stencils uniformly in space–time to increase efficiency in our mixed strategies for training neural stencil emulators.

(i) **Downsampled+Diff Init:** Combine downsampled stencils with a short simulation burst from a new initialization to the same stencil count.

(ii) **Downsampled+Extend:** Combine downsampled stencils with a short extension of the original simulation from its terminal state to the same stencil count.

(iii) **Downsampled+Random:** Combine downsampled stencils with an equal number of one-step evaluations of randomly generated stencils via uniform or Sobol’ sampling.

(iv) **Downsampled+PCA:** Combine downsampled stencils with an equal number of one-step evaluations of PCA-guided synthetic stencils generated with uniform or Sobol’ space filling design.

These four data augmentation choices yield four mixed strategies that combine the downsampled on-trajectory data with one of the pure strategies from Section 3.1.1. These mixes reduce redundancy while injecting state-space diversity. We use $\lambda = 0.5$ in experiments.

Remark (resolution scalability). As grid size (N) in state snapshot grows, the stencil dimension m and model $\hat{\mathbf{F}}_\theta$ can remain fixed while the number of available stencils Z scales proportional to N^2 . This resolution scalability further highlights strong few-shot learning aspect of our NSE approach.

4 Experiments

We test our Neural Stencil Emulator (NSE) on canonical PDEs to evaluate:

1. how sampling design affects data efficiency and forecast accuracy;
2. whether synthetic, PCA-guided designs improve few-shot generalization over on-trajectory and random space-filling baselines; and

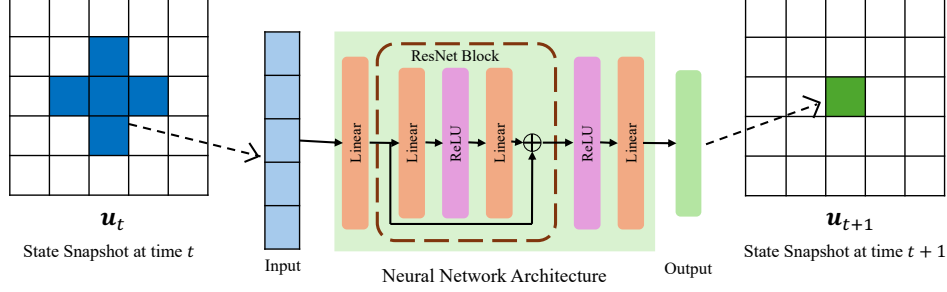


Figure 3: Residual network inspired neural network architecture used in our neural stencil emulator.

3. whether hybrids that mix decorrelated on-trajectory stencils with synthetic stencils offer the best robustness–efficiency trade-off.

NSE learns the discretized RHS from local inputs and is rolled out with an explicit integrator for forecasting. We evaluate on nonlinear PDEs—Allen-Cahn, Advection-Diffusion, and (scalar) Burgers’—to assess generalization to unseen initial conditions. Details of each PDE are in Appendix A.

Model architecture and training details. Our NSE uses a two-block residual network (Fig. 3) with 64-unit linear layers. It predicts time derivative, advanced via explicit Euler timestepping. We train with Adam (initial learning rate 0.01) with cosine decay schedule for 5,000 epochs.

Data and strategies. For *pure* strategies, we use a short run of 10 timesteps from one initial condition on a 32×32 grid, yielding 10,240 stencils for *Short-Traj* strategy. *Random* strategies draw 10,240 stencils from the PDE’s physically admissible range; *PCA-guided* strategies build 10,240 synthetic stencils by sampling in a principal-component space estimated from the short run and mapping them back to state space. For *mixed* strategies, we assume one full simulation of 1,000 timesteps over $t \in [0, 1]$ plus a small budget equivalent to 10 timesteps, which we allocate to (i) extending the trajectory (*Downsampled+Extend*), (ii) a short burst from a different initialization (*Downsampled+Diff Init*), or (iii) generating synthetic stencils (*Downsampled+Random*, *Downsampled+PCA*). In all mixed variants, we uniformly downsample the on-trajectory data to 10,240 stencils to reduce space–time correlation and combine them 1:1 with the synthetic/supplemental batch of 10,240 stencils yielding a total of 20,480 stencils. Under a small, fixed numerical solver budget, *mixed* strategies therefore train on twice as many stencils as *pure* strategies.

Evaluation protocol. We take 10 unseen initial conditions and evolve each with NSE trained under the pure or mixed strategies above. Performance is reported as the trajectory of log–RMSE between 2D snapshots from the full-order numerical solver and NSE over the rollout horizon.

Results. Figures 4, 5, and 6 summarize Allen-Cahn, Advection-Diffusion, and Burgers’, respectively, in a 2×3 layout: rows compare *Pure* vs. *Mixed* strategies; columns sweep diffusion coefficients $D \in \{5 \times 10^{-4}, 10^{-3}, 2 \times 10^{-3}\}$ from left to right. In Allen-Cahn system (Fig. 4), *PCA*-guided designs consistently outperform *Short-Traj* within the pure setting. Pure *Random* designs outperform both *PCA* and *Short-Traj* across all D values—especially at longer horizons where coverage of rare stencil configurations matters; within the Random and PCA families, Sobol’ low-discrepancy sampling typically slightly outperforms i.i.d. Uniform sampling.

In the mixed setting, *Downsampled+PCA* shows clear, substantial gains over its pure *PCA* counterpart across all D values. *Downsampled+Diff Init* and *Downsampled+Extend* also improve relative to their pure variants but generally trail *Downsampled+PCA*. *Downsampled+Random* offers only marginal gains over pure *Random*, likely because it does not exploit relationships in the on-trajectory data and downsampled stencils alone provide limited additional coverage. Overall, *Downsampled+PCA* and *Downsampled+Random* outperform *Downsampled+Diff Init* and *Downsampled+Extend*; within the mixed setting, we do not observe a consistent separation between Sobol’ and Uniform variants.

Why does Downsampled+PCA help? In mixed strategies, PCA is fit to a full trajectory (not a short burst), capturing a broader basis of stencil states and their correlations; the synthesized stencils then better target rare but dynamically important directions, yielding consistent gains over pure *PCA* and other mixed baselines. Uniform downsampling (*Extend/Diff Init*) adds little span, so their improvements are modest over *Short-Traj*. In the pure setting, PCA’s basis is narrow due to short run data—hence it performs worse than *Random* yet still better than *Short-Traj*.

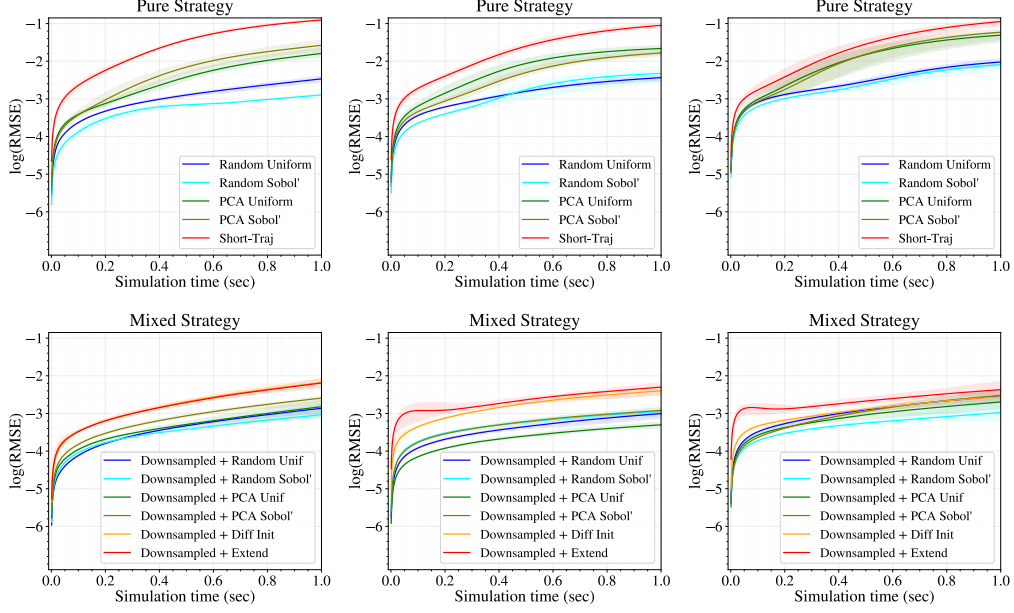


Figure 4: **Allen-Cahn system:** Neural stencil emulator’s PDE rollout errors across different strategies using 3 diffusion coefficients. Columns (left→right) use $D \in \{5 \times 10^{-4}, 10^{-3}, 2 \times 10^{-3}\}$; rows compare *Pure* vs. *Mixed* sampling strategies. Curves aggregate NSE solutions over 10 unseen initial conditions providing mean of \log -RMSE and the bands show $2\text{-}\sigma$ variability around that mean.

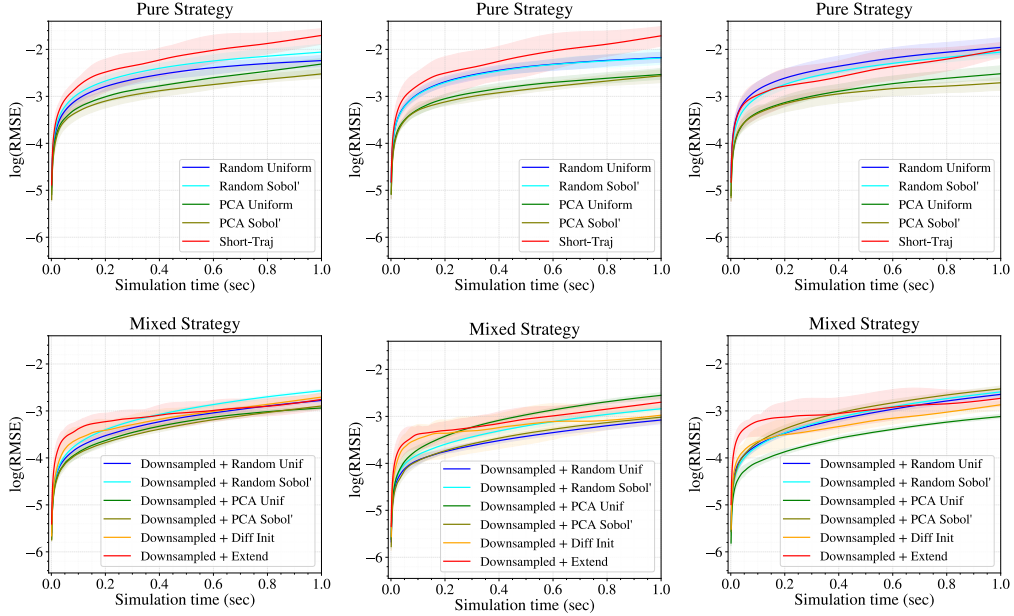


Figure 5: **Advection-Diffusion system:** Neural stencil emulator’s PDE rollout errors across different strategies using 3 diffusion coefficients. Columns (left→right) use $D \in \{5 \times 10^{-4}, 10^{-3}, 2 \times 10^{-3}\}$; rows compare *Pure* vs. *Mixed* sampling strategies. Curves aggregate NSE solutions over 10 unseen initial conditions providing mean of \log -RMSE and the bands show $2\text{-}\sigma$ variability around that mean.

In Advection-Diffusion system (Fig. 5), the *Pure* setting shows a clear ordering: *PCA*-guided designs are the best across the diffusion sweep, with *PCA-Sobol'* typically lowest error, followed closely by *PCA-Uniform*. Both *Random* variants trail the *PCA* designs, and *Short-Traj* (*Ergodic*) is consistently the worst. The separation is most pronounced at lower diffusion and narrows as D increases (rightward columns), but the *PCA* strategy’s lead persists throughout the horizon.

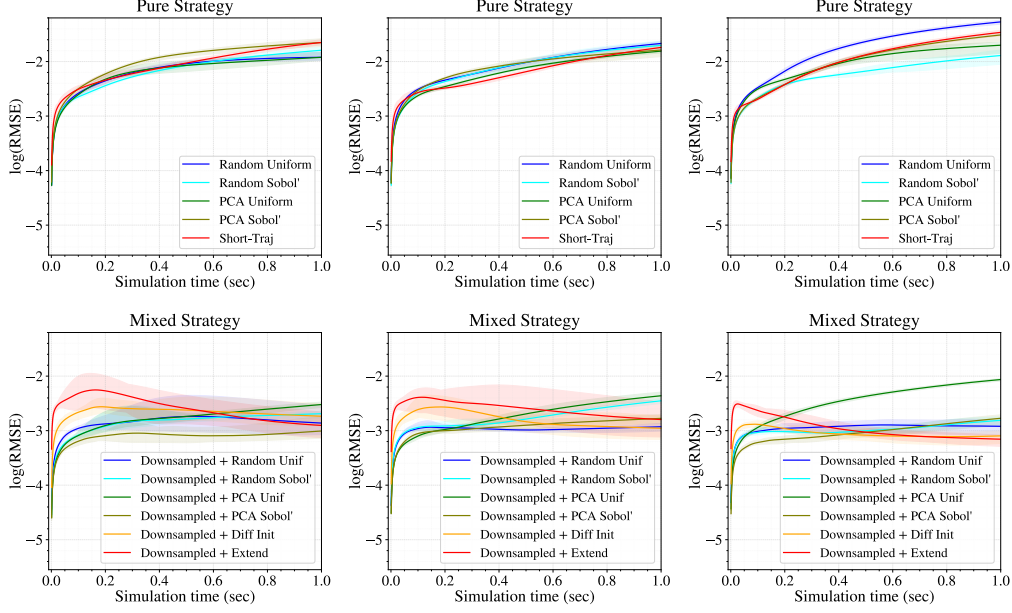


Figure 6: **Burgers' equation:** Neural stencil emulator's PDE rollout errors across different strategies using 3 diffusion coefficients. Columns (left→right) use $D \in \{5 \times 10^{-4}, 10^{-3}, 2 \times 10^{-3}\}$; rows compare *Pure* vs. *Mixed* sampling strategies. Curves aggregate NSE solutions over 10 unseen initial conditions providing mean of \log -RMSE and the bands show 2- σ variability around that mean.

In the *Mixed* setting, results are more nuanced. *Downsampled+PCA* does not uniformly dominate: depending on D , it is often among the top performers but is comparable to *Downsampled+Random*, with overlapping error bands for much of the rollout. *Downsampled+Diff Init* and *Downsampled+Extend* again lag, the remaining strategies highlighting importance of data augmentation. Overall, mixed strategies narrow the performance spread seen in the pure case; rankings vary with D and horizon length, and no consistent Sobol' vs. Uniform winner among the compared strategies emerges.

In scalar Burgers' equation (Fig. 6), the *Pure* panels show little separation across diffusion coefficients: trajectories and bands largely overlap, especially in the first two columns. In the last column, *Random-Sobol'* and *PCA-Uniform* exhibit slightly lower late-time errors. Overall, under our short-run budget, sampling choice has only a modest effect; long-horizon error appears to be dominated by shock dynamics rather than the specific pure sampler.

In the *Mixed* panels, error bands are visibly larger and rankings become diffusion-dependent. *Downsampled+PCA* does not uniformly dominate; *Downsampled+Random*, *Downsampled+Extend*, and *Downsampled+Diff Init* are often comparable with overlapping error bands. The spread widens at lower diffusion (stronger advection/sharper features); among the non-synthetic mixed variants, *Downsampled+Extend* and *Downsampled+Diff Init* frequently underperform relative to *Short-Traj*. These patterns suggest that the performance on Burgers' is sensitive to augmentation: injecting synthetic or off-trajectory stencils can shift the data distribution near shocks and amplify compounding rollout error. Overall, no single method consistently wins across columns in mixed setting.

5 Conclusion

In this work, we propose a space-filling, spatial-correlation-preserving, PCA-based data-augmentation strategy that generates localized stencil data and trains an NSE to learn PDE governing equations in a non-intrusive and sample-efficient (~ 10 timesteps' worth of simulation) manner. Our PCA-guided synthetic stencils enable accurate few-shot forecasts across Allen-Cahn, Advection-Diffusion, and Burgers' equations using limited snapshots under tight compute budgets. Operationalized via NSE, the approach consistently outperforms on-trajectory sampling, underscoring the value of independent, space-filling stencil sampling for robust, sample-efficient modeling of computer simulations.

References

- [1] Mrinal Kaushik, Rakesh Kumar, and G Humrutha. Review of Computational Fluid Dynamics Studies on Jets. *American Journal of Fluid Dynamics*, 5(3A):1–11, 2015.
- [2] Yan Li, Shengbing Yang, Fang Feng, and Kotaro Tagawa. A review on numerical simulation based on CFD technology of aerodynamic characteristics of straight-bladed vertical axis wind turbines. *Energy Reports*, 9:4360–4379, 2023.
- [3] Bin Wang, Xin Xie, and Lijuan Li. A Review on Aspects of Climate Simulation Assessment. *Advances in Atmospheric Sciences*, 26(4):736–747, 2009.
- [4] Kendall McGuffie and Ann Henderson-Sellers. Forty years of numerical climate modelling. *International Journal of Climatology: A Journal of the Royal Meteorological Society*, 21(9):1067–1109, 2001.
- [5] Miguel Cerrolaza, Sandra Shefelbine, and Diego Garzón-Alvarado. *Numerical methods and advanced simulation in biomechanics and biological processes*. Academic Press, 2017.
- [6] Lawrence C V Evans. *Partial Differential Equations*, volume 19. American Mathematical Society, 2022.
- [7] Randall J LeVeque. *Finite difference methods for ordinary and partial differential equations*. SIAM, 2007.
- [8] John C Strikwerda. *Finite difference schemes and partial differential equations*. SIAM, 2004.
- [9] F. Moukalled, L. Mangani, and M. Darwish. *The Finite Volume Method in Computational Fluid Dynamics: An Advanced Introduction with OpenFOAM® and Matlab*. Fluid Mechanics and Its Applications. Springer International Publishing, 2015.
- [10] HK Versteeg and W Malalasekera. *An introduction to computational fluid dynamics: the finite volume method*. Pearson Education, 2007.
- [11] Anders Logg, Kent-Andre Mardal, and Garth N Wells. *Automated solution of differential equations by the finite element method*. Springer, 2012.
- [12] Olek C Zienkiewicz and Robert L Taylor. *The finite element method for solid and structural mechanics*. Elsevier, 2005.
- [13] Jan S Hesthaven and Tim Warburton. *Nodal discontinuous Galerkin methods: algorithms, analysis, and applications*. Springer, 2007.
- [14] Bernardo Cockburn, George Em Karniadakis, and Chi-Wang Shu. The development of discontinuous Galerkin methods. *Discontinuous Galerkin methods*, pages 3–50, 2000.
- [15] Alfio Quarteroni and Alberto Valli. *Numerical approximation of partial differential equations*. Springer, Heidelberg, 2008.
- [16] Maziar Raissi, Paris Perdikaris, and George E Karniadakis. Physics-informed neural networks: A deep learning framework for solving forward and inverse problems involving nonlinear partial differential equations. *Journal of Computational physics*, 378:686–707, 2019.
- [17] Yohai Bar-Sinai, Stephan Hoyer, Jason Hickey, and Michael P Brenner. Learning data-driven discretizations for partial differential equations. *Proceedings of the National Academy of Sciences*, 116(31):15344–15349, 2019.
- [18] Johannes Brandstetter, Max Welling, and Thomas Wiatowski. Message passing neural PDE solver. In *International Conference on Learning Representations (ICLR)*, 2022.
- [19] Isaac E Lagaris, Aristidis Likas, and Dimitrios I Fotiadis. Artificial neural networks for solving ordinary and partial differential equations. *IEEE transactions on neural networks*, 9(5):987–1000, 1998.
- [20] Shengze Cai, Zhiping Mao, Zhicheng Wang, Minglang Yin, and George Em Karniadakis. Physics-informed neural networks (PINNs) for fluid mechanics: A review. *Acta Mechanica Sinica*, 37(12):1727–1738, 2021.
- [21] Kuang Luo, Jingshang Zhao, Yingping Wang, Jiayao Li, Junjie Wen, Jiong Liang, Henry Soekmadji, and Shaolin Liao. Physics-informed neural networks for PDE problems: a comprehensive review. *Artificial Intelligence Review*, 58(10):1–43, 2025.
- [22] Lu Lu, Pengzhan Jin, Guofei Pang, Zhongqiang Zhang, and George Em Karniadakis. Learning nonlinear operators via DeepONet based on the universal approximation theorem of operators. *Nature machine intelligence*, 3(3):218–229, 2021.

- [23] Zongyi Li, Nikola Borislavov Kovachki, Kamyar Azizzadenesheli, Burigede Liu, Kaushik Bhattacharya, Andrew Stuart, and Anima Anandkumar. Fourier Neural Operator for Parametric Partial Differential Equations. In *International Conference on Learning Representations (ICLR)*, 2021.
- [24] Aditi S. Krishnapriyan, Amir Gholami, Shandian Zhe, Robert Kirby, and Michael W Mahoney. Characterizing possible failure modes in physics-informed neural networks. *Advances in Neural Information Processing Systems (NeurIPS)*, 34, 2021.
- [25] Zhiping Mao and Xuhui Meng. Physics-informed neural networks with residual/gradient-based adaptive sampling methods for solving partial differential equations with sharp solutions. *Applied Mathematics and Mechanics*, 44(7):1069–1084, 2023.
- [26] Kejun Tang, Jiayu Zhai, Xiaoliang Wan, and Chao Yang. Adversarial adaptive sampling: Unify PINN and optimal transport for the approximation of PDEs. In *International Conference on Learning Representations (ICLR)*, 2024.
- [27] Levi D McClenny and Ulisses M Braga-Neto. Self-adaptive physics-informed neural networks. *Journal of Computational Physics*, 474:111722, 2023.
- [28] Zixue Xiang, Wei Peng, Xu Liu, and Wen Yao. Self-adaptive loss balanced physics-informed neural networks. *Neurocomputing*, 496:11–34, 2022.
- [29] Jie Wang, Xufeng Xiao, Xinlong Feng, and Hui Xu. An improved physics-informed neural network with adaptive weighting and mixed differentiation for solving the incompressible Navier–Stokes equations. *Nonlinear Dynamics*, 112(18):16113–16134, 2024.
- [30] Ricky TQ Chen, Yulia Rubanova, Jesse Bettencourt, and David K Duvenaud. Neural Ordinary Differential Equations. *Advances in neural information processing systems*, 31, 2018.
- [31] Deepak Akhare, Pan Du, Tengfei Luo, and Jian-Xun Wang. Implicit neural differentiable model for spatiotemporal dynamics. *Computer Methods in Applied Mechanics and Engineering*, 446:118280, 2025.
- [32] Christopher Rackauckas, Yingbo Ma, Julius Martensen, Collin Warner, Kirill Zubov, Rohit Supekar, Dominic Skinner, Ali Ramadhan, and Alan Edelman. Universal differential equations for scientific machine learning. *arXiv preprint arXiv:2001.04385*, 2020.
- [33] Pake Melland, Jason Albright, and Nathan M Urban. Differentiable programming for online training of a neural artificial viscosity function within a staggered grid lagrangian hydrodynamics scheme. *Machine Learning: Science and Technology*, 2(2):025015, 2021.
- [34] Dmitrii Kochkov, Jamie A Smith, Ayya Alieva, Qing Wang, Michael P Brenner, and Stephan Hoyer. Machine learning–accelerated computational fluid dynamics. *Proceedings of the National Academy of Sciences*, 118(21):e2101784118, 2021.
- [35] Sungduk Yu, Walter Hannah, Liran Peng, Jerry Lin, Mohamed Aziz Bhouri, Ritwik Gupta, Björn Lütjens, Justus C Will, Gunnar Behrens, Julius Busecke, et al. Climsim: A large multi-scale dataset for hybrid physics-ml climate emulation. *Advances in neural information processing systems*, 36:22070–22084, 2023.
- [36] Noah D. Brenowitz and Christopher S. Bretherton. Spatially Extended Tests of a Neural Network Parametrization Trained by Coarse-Graining. *Journal of Advances in Modeling Earth Systems*, 11(8):2728–2744, 2019.
- [37] Anthony M. DeGennaro, Nathan M. Urban, Balasubramanya T. Nadiga, and T. Haut. Model Structural Inference Using Local Dynamic Operators. *International Journal for Uncertainty Quantification*, 9:59–83, 2019.
- [38] Han Chen. Black-box Stencil Interpolation Method for Model Reduction. S.M. Thesis, Department of Aeronautics and Astronautics, Massachusetts Institute of Technology, 2012. Non-intrusive, data-oriented method combining with conventional intrusive model reduction techniques.
- [39] Aviral Prakash and Yongjie Jessica Zhang. Nonintrusive projection-based reduced order modeling using stable learned differential operators. *Computer Methods in Applied Mechanics and Engineering*, 442:117946, 2025.
- [40] Suryanarayana Maddu, Dominik Sturm, Bevan L Cheeseman, Christian L Mueller, and Ivo F Sbalzarini. Stencil-net for equation-free forecasting from data. *Scientific reports*, 13(1):12787, 2023.
- [41] Jun-Ting Hsieh, Shengjia Zhao, Stephan Eismann, Lucia Mirabella, and Stefano Ermon. Learning neural PDE solvers with convergence guarantees. In *International Conference on Learning Representations (ICLR)*, 2019.

- [42] Victor Churchill and Dongbin Xiu. Deep learning of chaotic systems from partially-observed data. *Journal of Machine Learning for Modeling and Computing*, 3(3), 2022.
- [43] Giovanni Caramia and Elia Distaso. A Practical Approach to Computational Fluid Dynamics Using OpenFOAM®, 2025.
- [44] Steven L Brunton, Joshua L Proctor, and J Nathan Kutz. Discovering governing equations from data by sparse identification of nonlinear dynamical systems. *Proceedings of the National Academy of Sciences*, 113(15):3932–3937, 2016.

A PDE Systems

A.1 Allen-Cahn System

The following system of equations describes the Allen–Cahn formulation:

$$\frac{\partial \mathbf{u}(\mathbf{x}, t)}{\partial t} = D \nabla^2 \mathbf{u}(\mathbf{x}, t) + 5(\mathbf{u}(\mathbf{x}, t) - \mathbf{u}(\mathbf{x}, t)^3) \quad \text{on } \Omega, \quad (3a)$$

$$\mathbf{u}(\mathbf{x}, t_0) \sim \text{GP}(m(\mathbf{x}), k(\mathbf{x}, \mathbf{x})) \quad \text{on } \Omega, \quad (3b)$$

$$\nabla \mathbf{u}(\mathbf{x}, t) = 0 \quad \text{on } \partial\Omega. \quad (3c)$$

Here D is the diffusion coefficient and $5(\mathbf{u}(\mathbf{x}, t) - \mathbf{u}(\mathbf{x}, t)^3)$ represents the source term. The GP represents the Gaussian process, used to generate the initial spatial field $\mathbf{u}(\mathbf{x}, t_0)$, and a zero-gradient boundary condition is imposed on the boundary $\partial\Omega$.

A.2 Advection-Diffusion System

The following system of equations describes the advection–diffusion formulation on the domain $\Omega = [0, L]^n$:

$$\frac{\partial \mathbf{u}(\mathbf{x}, t)}{\partial t} = -a \nabla \mathbf{u}(\mathbf{x}, t) + D \nabla^2 \mathbf{u}(\mathbf{x}, t) \quad \text{on } \Omega, \quad (4a)$$

$$\mathbf{u}(\mathbf{x}, t_0) \sim \text{GP}(m(\mathbf{x}), k(\mathbf{x}, \mathbf{x})) \quad \text{on } \Omega. \quad (4b)$$

$$\mathbf{u}(\mathbf{x} + L\mathbf{e}_i, t) = \mathbf{u}(\mathbf{x}, t) \quad \forall \mathbf{x} \in \partial\Omega, i = 1, 2, \dots, n \quad (4c)$$

Here D is the diffusion coefficient, a is the advection velocity, and \mathbf{e}_i denotes the unit vector along the i^{th} coordinate axis. The GP represents the Gaussian process, used to generate the initial spatial field $\mathbf{u}(\mathbf{x}, t_0)$, and a periodic boundary condition is imposed on the boundary $\partial\Omega$.

A.3 Scalar Burgers' System

The following system of equations describes the Scalar Burgers' formulation on the domain $\Omega = [0, L]^n$:

$$\frac{\partial u(\mathbf{x}, t)}{\partial t} = -\eta \nabla u(\mathbf{x}, t) + \nu \nabla^2 u(\mathbf{x}, t) \quad \text{on } \Omega, \quad (5a)$$

$$u(\mathbf{x}, t_0) \sim \text{GP}(m(\mathbf{x}), k(\mathbf{x}, \mathbf{x})) \quad \text{on } \Omega. \quad (5b)$$

$$u(\mathbf{x} + L\mathbf{e}_i, t) = u(\mathbf{x}, t) \quad \forall \mathbf{x} \in \partial\Omega, i = 1, 2, \dots, n \quad (5c)$$

Here ν is the viscosity, η is the scalar velocity, and \mathbf{e}_i denotes the unit vector along the i^{th} coordinate axis. The GP represents the Gaussian process, used to generate the initial spatial field $u(\mathbf{x}, t_0)$, and a periodic boundary condition is imposed on the boundary $\partial\Omega$.

B Limitations

We assume a model whose dynamics are fully governed by a stencil operator; training is performed offline; we do not enforce structure-preserving constraints (e.g., symmetries or conservation laws) on the learned stencil; and our data-augmentation strategy is static (i.e., no dynamic/active learning). Furthermore, NSE targets stencil-based system identification, but standardized benchmarks with ground-truth operators and physics-aware diagnostics are scarce. Our primary evaluation–rollout error (log-RMSE) on held-out initial conditions–provides useful signal yet only indirectly reflects physical fidelity (e.g., conservation, shock resolution, boundary fluxes). Although non-intrusive, NSE remains coupled to the discretization and time integrator; modeling and integration errors may be conflated, and transferability across grids, boundary conditions, and to 3D or multiphysics settings remains untested. Developing standardized operator-identification benchmarks and richer, physics-grounded metrics is an important direction for future work.